

Supporting Information for

Growth and one-dimensional heteroepitaxy of binary colloidal crystals

Jun Nozawa,^{†,*} Satoshi Uda,[†] Akiko Toyotama,[‡] Junpei Yamanaka,[‡] Hiromasa Niinomi,[†] Junpei Okada[†]

[†]Institute for Materials Research, Tohoku University, 2-1-1 Katahira, Aoba-ku, Sendai 980-8577, Japan

[‡]Graduate School of Pharmaceutical Sciences, Nagoya City University, 3-1 Tanabe, Mizuho, Nagoya, Aichi 467-8603, Japan

Correspondence to: nozawa@imr.tohoku.ac.jp

1. Effect of solution composition on the crystallized volume of each phase.

Figure S1 shows grown crystals of each phase under various solution conditions at a constant C_p of 1.0 g/L. At a solution composition of $A_{20}B_{80}$, the primary phase was A. After the development of A phase, the AB_2 phase grew in the intergranular spaces of A phase (Figure S1A). At a solution composition of $A_{15}B_{85}$, the primary phase was AB_2 . The AB_2 phase was the majority phase, followed by A phase (Figure S1B). At a solution composition of A_5B_{95} , the primary phase was B. Since the growth of the B phase shifted the solution towards an A-rich composition, AB_2 and A phases were formed around B phase grains (Figure S1C). The resultant structure of the binary system strongly depended on solution composition, in which the primary phase, secondary phase, grain size, grain gain, and volume ratio varied with the solution composition.

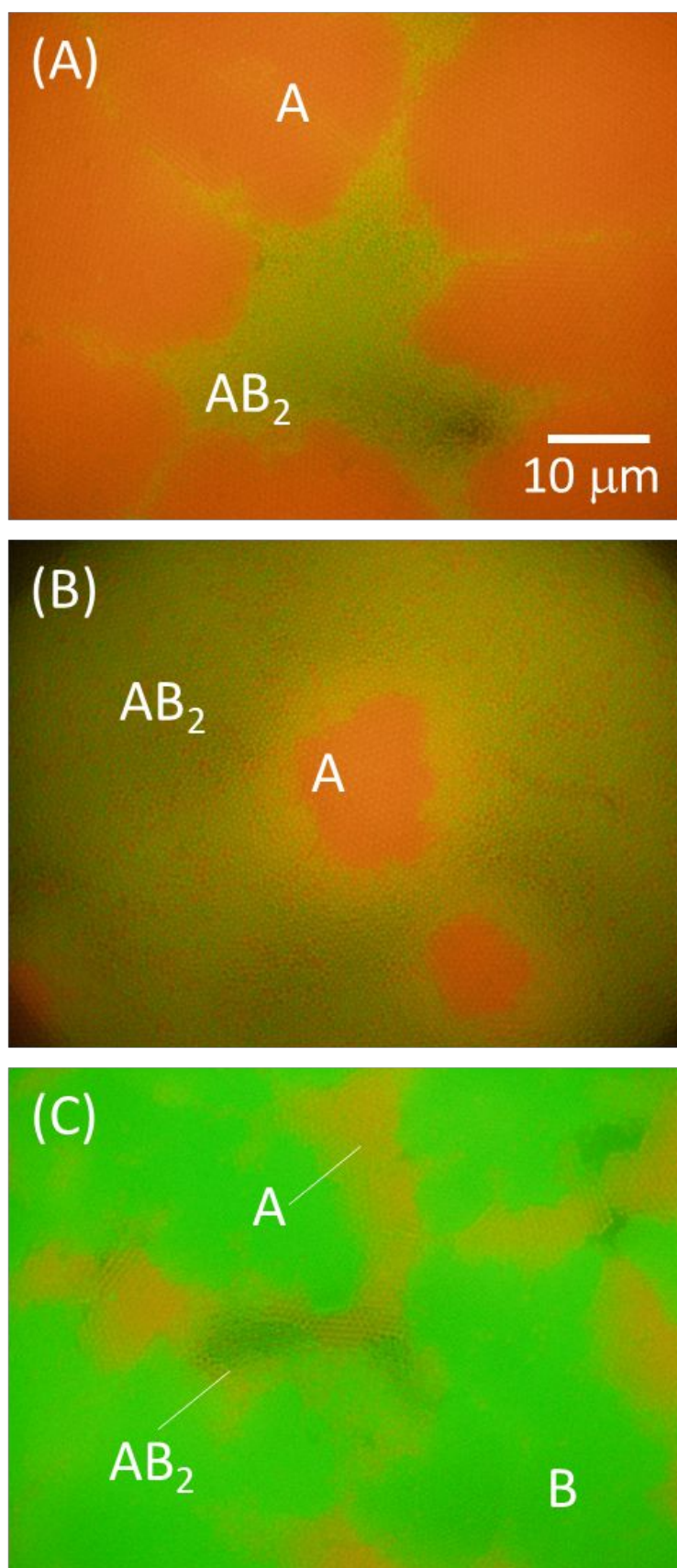


Figure S1. Formation of AB_2 superlattice structure at $C_p = 1.0$ g/L at various solution compositions: (A) $A_{20}B_{80}$, (B) $A_{15}B_{85}$, and (C) A_5B_{95} .

2. Area fraction during crystallization for different C_p .

Liquidus lines were drawn for the phase diagram in Figure 3A whose vertical axis is the inverse of the area fraction. Here, the area fraction, ϕ , is defined as the area of a particle divided by the observation area, which corresponds to the particle concentration. The ϕ at which nucleation occurred was measured for each C_p . Figure S2 shows images of the primary phase and solutions at $C_p = 0.75$, 1.25, and 1.5 g/L with the same solution composition of $A_{10}B_{90}$. The images were obtained soon after the nucleation of the primary phase. The ϕ at nucleation for $C_p = 0.75$, 1.25, and 1.5 g/L were 0.3, 0.25, and 0.15, respectively. As C_p increased the ϕ at nucleation decreased. The inverse of ϕ for $C_p = 0.75$, 1.25, and 1.5 g/L were 3.7, 4.0, and 6.7, respectively.

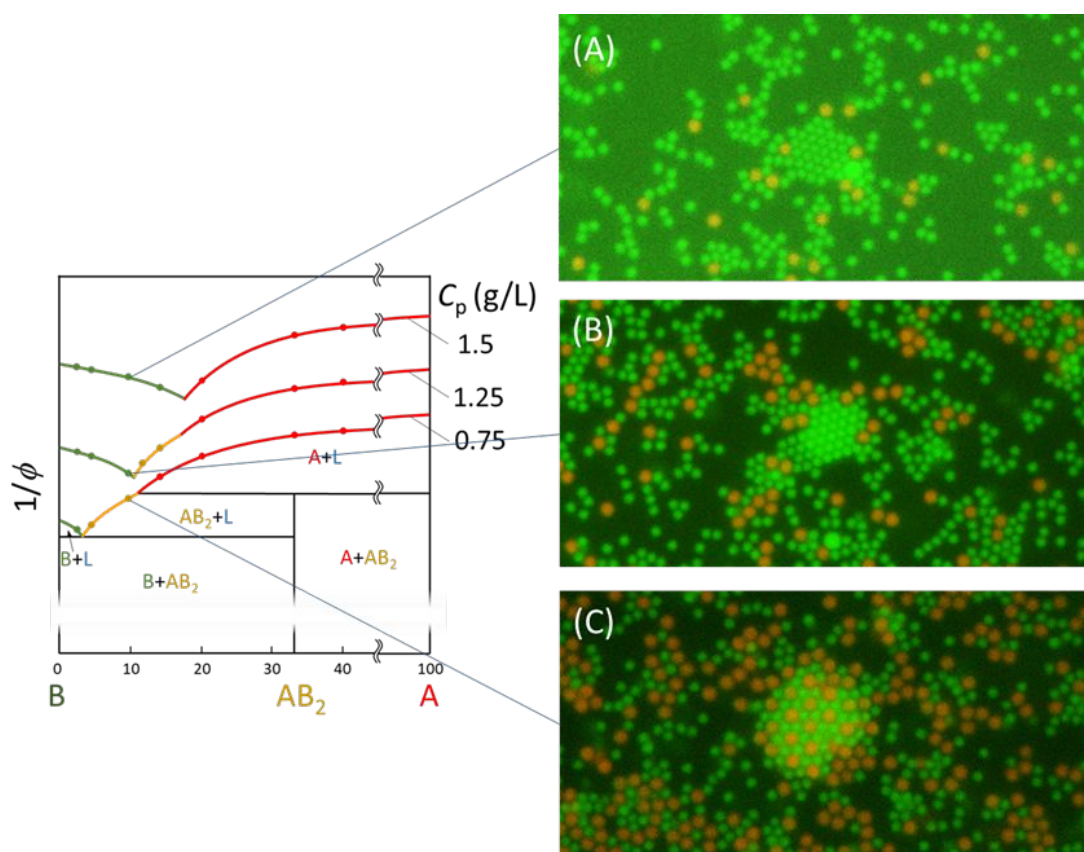


Figure S2. Area fraction, ϕ , at which nucleation occurred measured at various C_p : (A) 0.75, (B) 1.25, and (C) 1.5 g/L with the same solution composition of $A_{10}B_{90}$.

3. Calculation of interparticle potentials (van der Waals force and depletion attraction).

To compare particle interactions in the A, B, and AB₂ phases, interparticle potentials are evaluated. Since we have added a high concentration of charged polymers, 0.05–0.15 g/L, electrostatic repulsion is thought to be screened within a short distance. Thus, the particle interaction is predominantly induced by van der Waals (VDW) force and depletion attraction. The VDW potential between two spheres^{S1} is given by

$$U_{VDW}(r) = -\frac{A_H}{6} \left\{ 2a_p^2 \left(\frac{1}{r^2 - (2a_p)^2} + \frac{1}{r^2} \right) + \ln \frac{r^2 - (2a_p)^2}{r^2} \right\} \quad (S1)$$

where A_H is the Hamaker constant for a PS/water/PS system (1.4×10^{-20} J S²), a_p is the radius of particles, and r is the center-to-center distance between particles. The strength of the depletion attraction potential, $U_{AO}(r)$, was derived by Asakura-Oosawa^{S3} and Vrij^{S4}:

$$U_{AO}(r) = -n_b k_B T V_{OV}(r) \quad (2a_p \leq r \leq 2R_d) \quad (S2)$$

$$= 0 \quad (r > 2R_d) \quad (S3)$$

where n_b is the polymer number density, k_B is the Boltzmann constant, T is the absolute temperature, $V_{OV}(r)$ is the overlap volume of spheres whose radii is R_d , and R_d is the depletion radius which consists of the particle radius ($a/2$) and the radius of gyration of the polymer in water (R_g). Here, R_g was measured by static light scattering (SLS) to be 220 nm. The value of n_b is obtained by the polymer number density at which the polymer coils overlap ($n_b^* = 3/4pR_g^3$) and the weight percent of polymer. $V_{OV}(r)$ is derived as

$$V_{OV}(r) = \frac{4\pi}{3} R_d^3 \left[1 - \frac{3r}{4R_d} + \frac{1}{16} \left(\frac{r}{R_d} \right)^3 \right]. \quad (S4)$$

The sum of the VDW force and depletion attraction with particle separation is drawn in Fig. S3. Based on the calculated interparticle potentials, the particle interactions of

each phase are compared. Here, a pair of A particles is denoted as A-A. When C_p is 0.075 g/L, the particle distances of A-A, A-B, and B-B for the A, AB₂, and B phases, respectively, are 100 nm (the particle distance is described in Fig. 5(I) in the manuscript), and that of B-B in the AB₂ phase is 200 nm. The particle potentials for A-A, A-B, and B-B at a distance of 100 nm are -0.70 , -0.56 , and -0.44 $k_B T$, respectively, and for B-B at a distance of 200 nm it is -0.16 $k_B T$. When we focus on three particles in each phase, as shown in Fig. 3C in the manuscript, $3\varepsilon_{AA}$ (2.10 $k_B T$) > $3\varepsilon_{BB}$ (1.32 $k_B T$) > $2\varepsilon_{AB} + \varepsilon_{BB'}$ (1.28 $k_B T$), is confirmed. This result supports the conclusion that the variation of free energy with polymer concentration is at its smallest in the AB₂ phase.

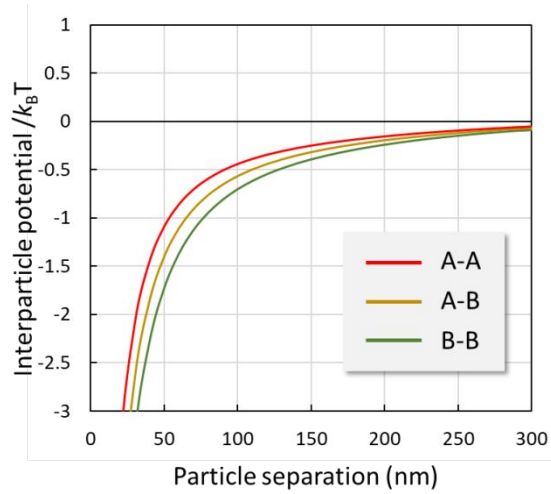


Figure S3. Calculation of interparticle potentials (wan der Waals force and depletion attraction) for A-A, A-B, and B-B particle pairs.

4. Formation of binary colloidal crystals at various particle combinations.

Binary systems with size ratios α (small/large) outside the range shown in Figure 4 were also investigated. At $\alpha = 0.86$ (600/700), an fcc structure with a random configuration of large and small particles was formed since the large and small particles were similar (Figure S4A). At $\alpha = 0.54$ (380/700), which is a lower α value than that

shown in Figure 4, an AlB_2 -type phase was observed (Figure S4B). In the AB_2 structure described in the manuscript, large and small particles were aligned in the same plane. In contrast, large and small particles formed different layers in the AlB_2 -type structure (schematic illustration is shown in the inset of Figure S4B). The small particles were located at voids formed by three large particles. AB_{13} was expected to form at $\alpha \sim 0.5$ in the hard-sphere system, but it was not observed in the present study. The AB phase was also expected to form at lower α values, but it was not investigated in the present study and will be investigated in the future.

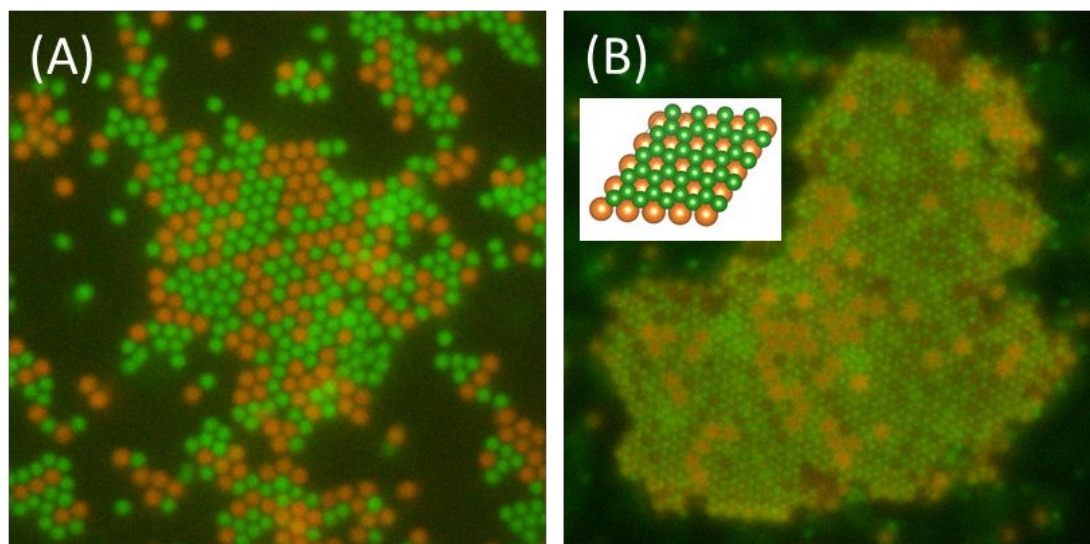


Figure S4. BCCs composed of 600 and 700 nm (A), and 380 and 700 nm (B) particles. Inset is a schematic illustration of the AlB_2 structure.

5. One-dimensional (1D) heteroepitaxial growth with different particle sizes.

1D heteroepitaxial growth occurred at various BCC particle combinations. Figure S4A shows the 1D heteroepitaxial growth in a binary system containing particle sizes of 380 and 500 nm. The relationship between the orientation of A and AB_2 was the same as in Figure 5(B) and (D). Figure S4B shows the growth of AB_2 (A: 790 nm, B: 600 nm) on A phase, which was the same type shown in Figure 5B and D. Type (C)

and (D) were also observed in each binary system. 1D heteroepitaxial growth was shown to occur at various combinations of BCC particle sizes.

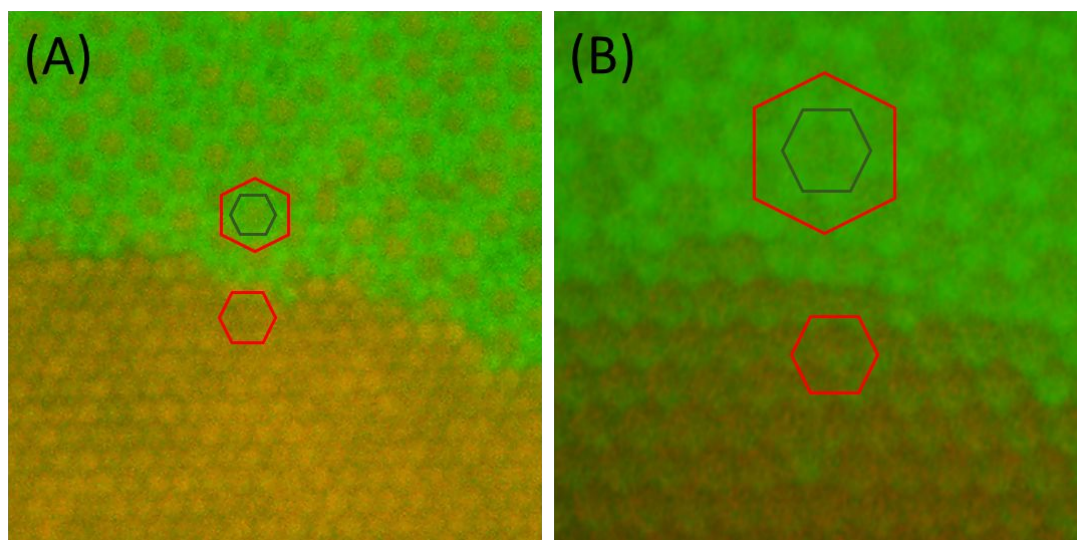


Figure S5. (A) One-dimensional (1D) heteroepitaxial growth of AB_2 phase (A: 500 nm, B: 380 nm) grown at $A_{15}B_{85}$ and $C_p = 1.5$ g/L. (B) AB_2 phase (A: 790 nm, B: 600 nm) grown at $A_{10}B_{90}$ and $C_p = 0.75$ g/L.

6. Effect of lattice mismatch on one-dimensional (1D) heteroepitaxial growth.

Figure S6 shows magnified images of the interface between the substrate and the epitaxial phase in Figure 5 (B) and (C). Their lattice constants were measured and showed that the lattice mismatch of (B) was much smaller than that of (C). As indicated by the dot, the lattice of the substrate and the epitaxial phase were well matched for (B) but not for (C). Since C_p for (C) was lower (0.75 g/L) than that of (B) (1.0 g/L), the lattice mismatch was due to fewer particle interactions.

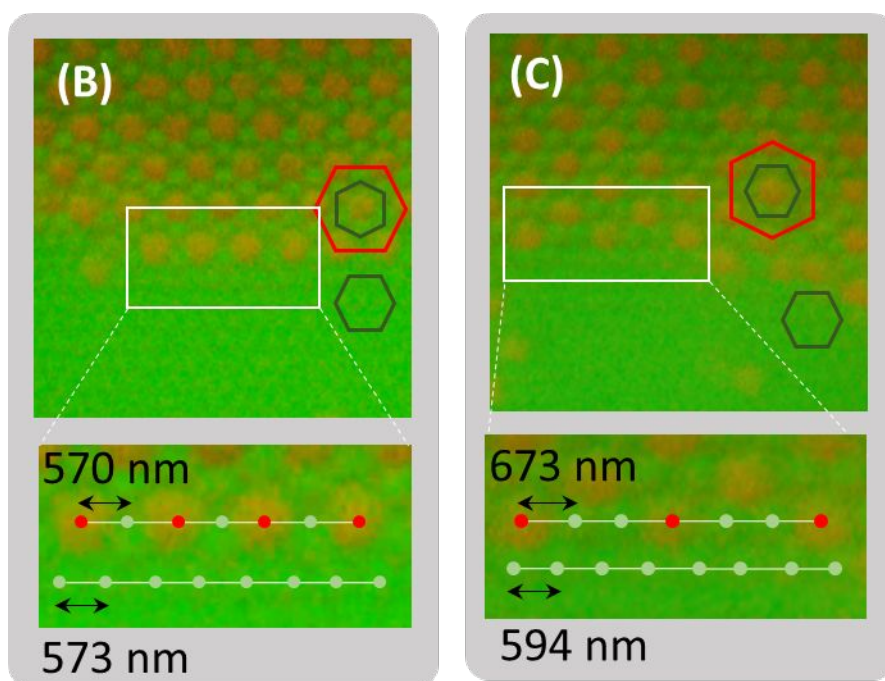


Figure S6. Schematic illustration of the lattice mismatch between AB_2 and B phase for Figure 5(B) and (C) in the manuscript.

7. One-dimensional heteroepitaxial growth of A on AB_2 phase.

In the manuscript, the nucleation of AB_2 on A or B is described. The nucleation of A phase on AB_2 was also observed *in-situ* (Figure S7). The formation of B phase on AB_2 also occurred at B-rich compositions, but it was rarely observed. As the AB_2 phase grew, B particles were consumed from solution at a rate two times higher than A particles. Thus, the environment near the crystal shifted towards an A-rich composition, and the nucleation of A phase was induced on the edge of the AB_2 phase.

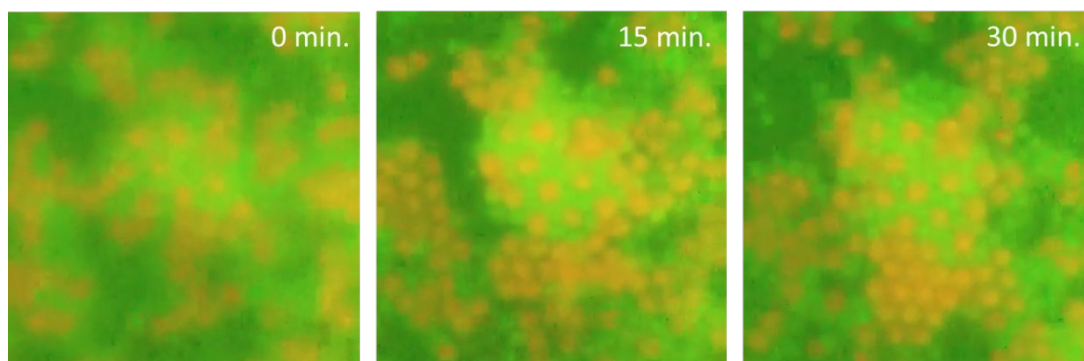


Figure S7. Nucleation of A phase on AB₂ phase via heteroepitaxial growth.

Supplementary references

(S1) Russel, W. B., Saville, D. A. & Schowalter, W. R. Colloidal Dispersions (Cambridge University Press: New York, 1989).

(S2) Israelachvili, J. Intermolecular and Surface Forces, 2nd ed.; Academic Press: London, 2011; Chapter 6.

(S3) Asakura, S.; Oosawa, F. On Interaction between Two Bodies Immersed in a Solution of Macromolecules. J. Chem. Phys. 1954, 22, 1255–56.

(S4) Vrij, A. Polymers at Interfaces and the Interactions in Colloidal Dispersions. Pure Appl. Chem. 1976, 48, 471–83.